

Scanning-free grazing emission x-ray fluorescence by means of an angular dispersive arrangement with a two-dimensional position-sensitive area detector

Y. Kayser,^{1,a)} J. Szlachetko,^{1,2} and J. Sà¹

¹Paul Scherrer Institut, 5232 Villigen-PSI, Switzerland

²Institute of Physics, Jan Kochanowski University, 25-406 Kielce, Poland

(Received 2 October 2013; accepted 16 November 2013; published online 6 December 2013)

We report on the application of a two-dimensional position-sensitive area detector towards grazing emission x-ray fluorescence (GEXRF) spectroscopy. GEXRF allows for surface-sensitive studies with nanometer-scale accuracy in the depth direction by measuring the intensity variation of an x-ray fluorescence line with the grazing emission angle. The presented experimental setup is based on a fixed sample-detector arrangement and does not require any moving components. We show that the dispersion of the grazing emission angle along a position-sensitive detector allows to acquire with an excellent angular resolution a full GEXRF profile in a single measurement. Moreover, the use of a two-dimensional detector allows to perform experiments with an increased solid angle of detection per emission angle. This results in combination with the nonsequential and simultaneous acquisition of the GEXRF profiles of different emission lines in considerably reduced acquisition times. The realization, the demands, and the main characteristics of the scanning-free GEXRF setup will be presented. A few experimental examples will serve to illustrate the analytical possibilities offered by the presented setup. © 2013 AIP Publishing LLC. [<http://dx.doi.org/10.1063/1.4838575>]

I. INTRODUCTION

The efficiency of surface analysis by means of x-ray probing combined with x-ray emission spectroscopy (XES) is limited by the rather large penetration depth of the incident x-rays into the sample. Surface sensitive analysis is of interest in different scientific and technological applications in which the physical properties of a material are modified by a layer deposition on the top of a surface or a doping process of the near-surface region. Sample depths of several nanometers up to at most a couple of hundred nanometers are affected. The down scaling of devices increases the importance and demands on surface speciation. In order to preserve a constant aspect ratio the sample volumes to be studied get shallower and the dopant concentrations are reduced. The surface region is also of interest for catalysis. However, in the hard x-ray energy range the typical attenuation length is in the micrometer range. Consequently, the XES signal which is recorded with standard emission spectroscopy setups originates not only from the sample surface but also from the bulk volume below the surface. Thus, the signal from the surface-near volume is dominated by the background contribution from the bulk volume. In order to enhance the surface sensitivity, either the incidence angle of the probing x-ray beam or the emission angle at which the XES signal is recorded has to be reduced to grazing angles, i.e., to angles close to the critical angle for total external reflection. The latter depends on the energy of the incident, respectively, emitted x-ray photons and the sample material. In grazing incidence x-ray fluorescence (GIXRF)^{1–5} the excitation of the XES signal is confined to the surface-near volume by reducing the incidence angle of the probing beam

to grazing values, while in grazing emission x-ray fluorescence (GEXRF)^{6–8} a detection setup which is only sensitive to x-rays emitted at grazing angles allows to record solely the XES signal from the surface-near volume.

A. Comparison of GIXRF and GEXRF

Both, GIXRF and GEXRF (Fig. 1), can be applied to the elemental depth-sensitive characterization on a nanometer-scale of the surface-near sample volume. The results provided by the two techniques can be expected to be identical if the energy of the x-rays which are incident at grazing angles is the same as the energy of the x-rays emitted at identical grazing angles.⁹ The physical equivalence of both techniques can be demonstrated with the principle of microscopic reversibility and reciprocity.¹⁰ An experimental evidence of the reciprocity was given by the observation of interference fringes in the angular dependence of the fluorescence radiation in GEXRF conditions.¹¹ From an experimental point of view, the differences between the two grazing geometries are on one side due to the different energies of interest for the acquisition of the angular dependence of the XES intensity and on the other side to the different solid angle of detection which is larger for GIXRF setups. The energy of interest is in GIXRF the one of the incident x-ray photons and in GEXRF the one of the emitted x-ray photons, thus once above and once below the absorption edge. The probed depth range scales therefore differently with the grazing angle in GIXRF and GEXRF because of the different absorption sensitivities to the sample matrix. The smaller solid angle of detection of GEXRF setups is caused by the fact that the angular acceptance of the detection setup has to be reduced in order to have well-defined observation angles. On the other hand, this allows

^{a)}Author to whom correspondence should be addressed. Electronic mail: yves.kayser@psi.ch

to combine the grazing emission geometry either with low-energy resolution detectors or with high-energy resolution detection setups without further deteriorating the solid angle of detection.^{12–15}

B. Depth-sensitivity of GEXRF

The surface- and depth-sensitive character of GEXRF (and also of GIXRF) can be explained by two factors, the first being the increased x-ray absorption in the depth direction caused by the shallow emission angles, the second being the refraction of the x-rays at the interface formed by the sample with the surrounding environment (air, gas, or vacuum). Because of the latter factor the refracting interface has to be flat on an x-ray wavelength scale. Since for x-rays the real part of the complex refractive index is smaller than unity by a decrement factor which is of the order of 10^{-7} to 10^{-3} , the angle subtended between the x-ray path and the sample-environment interface will always be smaller on the sample side (Fig. 1). Consequently, x-rays emitted from the bulk sample volume cannot be detected if the grazing emission angle is sufficiently small, i.e., below the critical angle (Fig. 1, bottom panel). The detected XES signal is due to an evanescent wave propagating along the sample surface.⁹ The probed depth region is a few nanometers wide and only the atoms located close to the sample surface contribute to the detected XES yield. In the vicinity of the critical angle, the depth range to which the experimental setup is sensitive changes signif-

icantly and increases from a few to several hundred nanometers. In addition to the XES signal from the surface-near atoms, also the XES signal of atoms located further away from the surface can be detected after refraction at the interface. In the angular range above the critical angle the probed depth region increases, in a first approximation, linearly with the emission angle and the sample depth which is probed at a given emission angle is mainly limited by the absorption of the emitted x-rays. Recording the XES intensity as a dependence of the grazing emission angle allows then to characterize the in-depth distribution on a nanometer-scale of the atoms emitting the measured XES signal. In this respect, the grazing angle at which the emitted x-rays are detected has to be well controlled. In comparison to other surface-sensitive analytical techniques, GEXRF measurements performed with hard x-rays allow for non-destructive micro-trace, surface-sensitive, and depth-profiling experiments on multielemental samples and require little or no sample preparation. Thus, GEXRF experiments can be realized under atmospheric pressure, allowing for non-invasive *in situ* experiments at ambient conditions.

C. GEXRF excitation source

With respect to GIXRF, the main experimental advantage offered by GEXRF is the independence on the excitation source. Indeed, GIXRF measurements can only be realized with collimated, monochromatic x-ray beams in order to preserve the angular resolution, whereas GEXRF experiments can be performed with different types of excitation sources for the XES signal in terms of ionizing particles (x-rays or charged particles), energy bandwidth of the ionizing particles, and spatial size of the ionizing beam.^{16–20} The GEXRF profiles and thus also the depth ranges probed at different grazing emission angles are essentially determined by the energy of the emitted x-rays and the sample matrix. This is especially of advantage if absorption measurements are realized in the grazing emission geometry. Indeed, in GIXRF the critical angle and the probed depth range vary pronouncedly when the incident beam energy is scanned through an absorption edge,²¹ while in GEXRF both parameters are independent of the incident beam energy.¹³ Sample thickness effects can be excluded in an absorption spectrum measured in the GEXRF configuration since the attenuation depth of the incident beam is always larger than the probed depth. Only if the XES signal is excited with low-energy charged particles which penetrate less deep than the depth range probed by GEXRF at the largest covered emission angle, an influence on the GEXRF profiles becomes noticeable. Moreover, as we will demonstrate, a spatially resolved detection of the emitted x-ray photons allows to acquire GEXRF profiles in a single measurement without scanning through different sample-detector orientations. This is a further, considerable advantage offered by the GEXRF geometry. Note that in GIXRF the angular dependence cannot be reconstructed from a measurement of the XES signal at a single sample position and the angular intensity profile has to be recorded sequentially by varying the incidence angle.

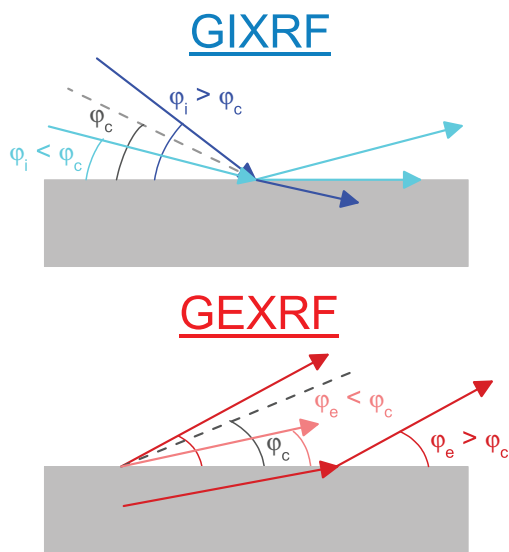


FIG. 1. In the grazing incidence geometry, the total external reflection of x-rays at incidence angles φ_i below the critical angle φ_c not only improves the excitation efficiency for fluorescence radiation of the near-surface region but also prevents in addition any fluorescence excitation of the bulk. Above the critical angle φ_c , the probed depth region is limited by the x-ray absorption. In the grazing emission geometry, the probing beam penetrates into the sample and the XES signal is created, both, at the surface and in the bulk volume. However, for grazing emission angles φ_e below the critical angle φ_c only the XES signal excited at the surface can be observed, all contributions from the bulk are suppressed by the refraction at the sample surface interface. For emission angles above the critical angle, the probed depth volume increases with the emission angle and the XES signal emitted by atoms located further away from the surface becomes observable.

D. Scanning-free GEXRF concept

In state-of-the-art GEXRF setups, the XES intensity dependence on the grazing emission angle has to be recorded in a series of sequential measurements. The emitted XES signal has to be measured at different sample or detector positions which correspond to different grazing angles, the quality of the measurement depending on the accuracy, and the resolution of the positioning system. Indeed, a good angular resolution, i.e., of the order of a few hundredth degree or even better, has to be ensured in order to resolve eventual sharp interference fringes in the angular intensity profile.²² The required angular resolution depends on the fluorescence line and the sample under investigation, e.g., for layered samples the period of the interference fringes varies inversely with the energy of the emitted x-rays and the layer thickness.¹⁰ The main factor influencing the instrumental angular resolution is the angular aperture of the GEXRF detection system. Equivalently to the sample orientation, also the detector position can be modified in order to change the grazing emission angle. Indeed, in GEXRF, a spatially resolved measurement of the XES signal allows to record the dependence of the XES intensity on the grazing angle, the angle being defined by the position of the detector with respect to the sample surface. In order to refine the angular resolution, the angular acceptance of the detection setup is optimized by means of a slit system or a dispersion device.

The possibility of recording an angular intensity profile in GEXRF without scanning through the sample or the detector positions was first demonstrated by means of an imaging plate in 1993 by Sasaki.²³ A following application was to acquire positional information about radioisotopes on the top of a reflecting surface by recording the interference pattern under grazing emission conditions of the x-rays emitted during electron capture processes.²⁴ Other GEXRF setups and experiments reported in the literature were, to the best of our knowledge, performed only in a sequential approach by measuring the XES intensity successively at different sample-detector orientations. Compared to two-dimensional pixel detectors, imaging plates are advantageous in terms of detection area and spatial resolution. Both of these aspects are of importance for GEXRF, once because of the covered range in grazing emission angles and once because of the angular resolution. The covered range in emission angles should range from 0° to twice or even thrice the critical angle. However, with respect to imaging plates, modern position-sensitive detectors offer advantages in terms of sensitivity, signal-to-noise ratio, the dynamic range and the linearity in the intensity response. The latter two aspects are of special importance since the x-ray intensity varies significantly with the grazing emission angle. Moreover, the x-ray intensities are acquired in a digitized way which facilitates data treatment and analysis.

In the present work, a scanning-free GEXRF setup will be presented which is based on the dispersion of the grazing emission angle along one of the dimensions of a two-dimensional position-sensitive pixel detector and which allows therefore to acquire the angular intensity profile of the XES signal in a single measurement at a fixed position of the setup components. Instability effects due to source in-

tensity fluctuations or motor vibrations are avoided. The angular acceptance in the direction along which the emission angle is dispersed is defined by the individual pixels, no slit system is required. The XES intensity is recorded simultaneously for the different covered grazing emission angles, eliminating any dead time caused by scanning through different motor positions. Measurements with different sample types, namely bulk, layered, and ion-implanted samples, will be shown. The detector extension perpendicular to the angular dispersion axis permits to circumvent the most important disadvantage of existing GEXRF arrangements, the small solid angle of detection.

II. METHODOLOGY AND INSTRUMENTATION

The experimental setup was realized at the Optics beamline of the Swiss Light Source (SLS).²⁵ The synchrotron radiation was produced by a bending magnet, monochromatized by a cryogenically cooled Si(111) channel cut monochromator and focused down to approximately $200 \times 150 \mu\text{m}^2$ ($v \times h$) with a bendable toroidal mirror (1:1 focusing). The samples were mounted on a goniometer head and oriented at a fix shallow incidence angle which was sufficiently far above the critical angle of total external reflection for the considered synchrotron beam energies. A reference sample holder was used to ensure that the different samples were at the same position with respect to the incident beam and the two-dimensional position-sensitive area detector, a PILATUS 100 K area detector.²⁶ The reasons to choose a shallow incidence angle for the incident x-ray beam were, first, to disperse the incident beam on the sample surface in order to excite the XES signal in a larger surface area and, second, to enhance the excitation of the XES signal from the near-surface region with respect to the bulk contribution and avoid background contributions from the bulk volume. This resulted in improved background conditions. Indeed, for shallow incidence angles the probed depth region is not only limited by the extinction depth of the XES signal but also by the attenuation depth of the incident synchrotron beam.

The XES signal produced in the sample was recorded with the PILATUS 100 K area detector which is a single-photon counting detector and allowed for a position-sensitive detection of the photon intensity by storing for each pixel the number of photons with an energy above the detector threshold. The detector array consisted of $n_H \times n_V = 487 \times 195$ pixels with a size of $172 \times 172 \mu\text{m}^2$ (active area $83.8 \times 33.5 \text{ mm}^2$) and was positioned so that the normal to the detector surface was perpendicular to the incident beam direction and parallel to the sample surface plane, one of the detector dimensions being parallel to the latter plane (see Fig. 2). The orientation close to 90° with respect to the synchrotron beam minimized the scattering background on the detector whereas the detected XES yield is not affected since the fluorescence x-ray photons are emitted isotropically by the source atoms.

The emission angle scale was hence dispersed along the detector dimension which is vertical to the sample surface plane. In a pixel column of the detector the different detector pixels subtend each a different, discrete angle with

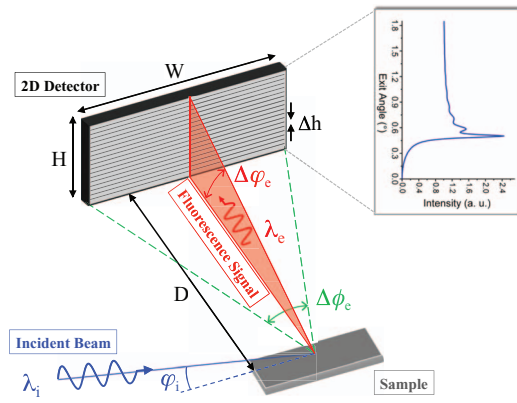


FIG. 2. Illustration of the scanning-free GEXRF setup. The dispersion of the grazing emission angle along one direction (in the illustration, the vertical one) of the position-sensitive detector allows to acquire the GEXRF intensity profile at once without moving any components. An exemplary angular profile of the emitted fluorescence intensity for a single emission line from a thin layered sample is displayed on the right. The covered angular range $\Delta\varphi_e$ and the angular resolution depend on the sample-to-detector distance D , the detector height H , and the vertical pixel size Δh (see also Fig. 3). The second direction (in the illustration, the horizontal one of width W) allows to acquire the emitted x-ray fluorescence intensity for each emission angle with an increased solid angle of detection per grazing emission angle. The synchrotron beam was incident at a shallow angle on the sample in order to enhance the excitation of the XES signal in the near surface region.

respect to the sample surface. Thus, the position-sensitive detection allows to discriminate the emission angles of the different recorded x-ray photons. A prerequisite is of course that the angular stepping in the vertical direction along which the grazing emission angles are dispersed should be fine enough, i.e., the difference in the emission angle between two successive pixels, or equivalently the opening angle per pixel, should be sufficiently small to provide a good angular resolution. This can be achieved, for a fixed pixel size, by increasing the sample-to-detector distance D . A good angular resolution is required to separate eventual interference fringes in the angular XES intensity profile, e.g., for layered samples.^{10,11,27}

The detector dimension parallel to the sample surface plane permitted to increase the solid angle of detection for the different emission angles. The angular intensity profiles recorded in each pixel column were merged together by summing the intensities along each horizontal pixel row. The whole active area of the detector was thus used. Consequently the overall acquisition time could be notably reduced, permitting to acquire a full GEXRF profile in a relatively short time period. The emission angle varied, however, slightly in the horizontal direction along a row of pixels since the distance to the XES source point on the sample surface varies because of the plane detector surface. However, the horizontal variation in the emission angle drops quickly with the sample-to-detector distance and becomes smaller than the average spanned opening angle per pixel in the vertical direction (Fig. 3, lower right panel). Finally, the contribution to the angular resolution when binning the values in the different columns is for sample-to-detector distances larger than 80 cm about an order of magnitude smaller than the contribution of the pixel size. In the acquired grazing emission XES intensity

profile, the mean emission angle value of each horizontal row was assigned to the binned intensity value. A relatively large sample-to-detector distance is, thus, not only required to resolve the emission angle in the vertical direction but also to avoid an important spread in the emission angle value along the horizontal direction and consequently a blurring of the angular resolution when binning.

The covered range of emission angles should be broad enough, i.e., at least twice the critical angle, to acquire useful angular XES intensity profiles at once without moving any components. Moreover, the solid angle per covered emission angle unit should be large enough to ensure that the measurements can be performed in a short time interval. Although the XES intensity is monitored simultaneously for all the different emission angles, the solid angle per covered emission angle is referred to instead of the overall solid angle of detection. This allows for a better comparability with respect to standard grazing incidence or grazing emission setups where the XES dependence on the grazing angle is recorded sequentially in a point-by-point angular scan. The shorter dimension of the PILATUS detector allowed to cover a large enough angular range, the solid angle per emission angle could be increased by orienting the long side parallel to the sample surface and thus by binning the intensities recorded in each row over a larger number of pixels.

The covered range in emission angles is determined by the detector dimension ($H = n_V \Delta h$) and can be calculated with the following formula:

$$\Delta\varphi_e = \tan^{-1} \left(\frac{n_V \Delta h}{D} \right), \quad (1)$$

where $\Delta h = 172 \mu\text{m}$ corresponds to the pixel size in the vertical direction. The opening angle for pixel $j = 1, \dots, n_V$ along the emission angle dispersion axis is given by

$$\delta\varphi_e = \tan^{-1} \left(\frac{j \Delta h}{D} \right) - \tan^{-1} \left(\frac{(j-1) \Delta h}{D} \right), \quad (2)$$

whereas the emission angle was set to the value corresponding to the pixel center,

$$\varphi_e = \tan^{-1} \left(\frac{(j-0.5) \Delta h}{D} \right). \quad (3)$$

The above equations are valid for the pixel column which faces directly the spot irradiated by the probing beam on the sample surface. As it was already mentioned, a different sample-to-detector distance has to be considered for the pixels in other detector columns: $D \rightarrow \sqrt{D^2 + (k \Delta h)^2}$ with $k = -\frac{n_H-1}{2}, \dots, \frac{n_H-1}{2}$ where it is assumed that the incidence point of the probing beam on the sample surface is centered along the horizontal detector dimension. The solid angle of detection per emission angle (i.e., per pixel row) with respect to a point source corresponds to

$$\Omega_e = 4 \times \tan^{-1} \left(\frac{n_H \Delta h}{2D_j \sqrt{4D_j^2 + \Delta h^2 + (n_H \Delta h)^2}} \right), \quad (4)$$

$$\text{with } D_j = \sqrt{D^2 + (j \Delta h)^2}.$$

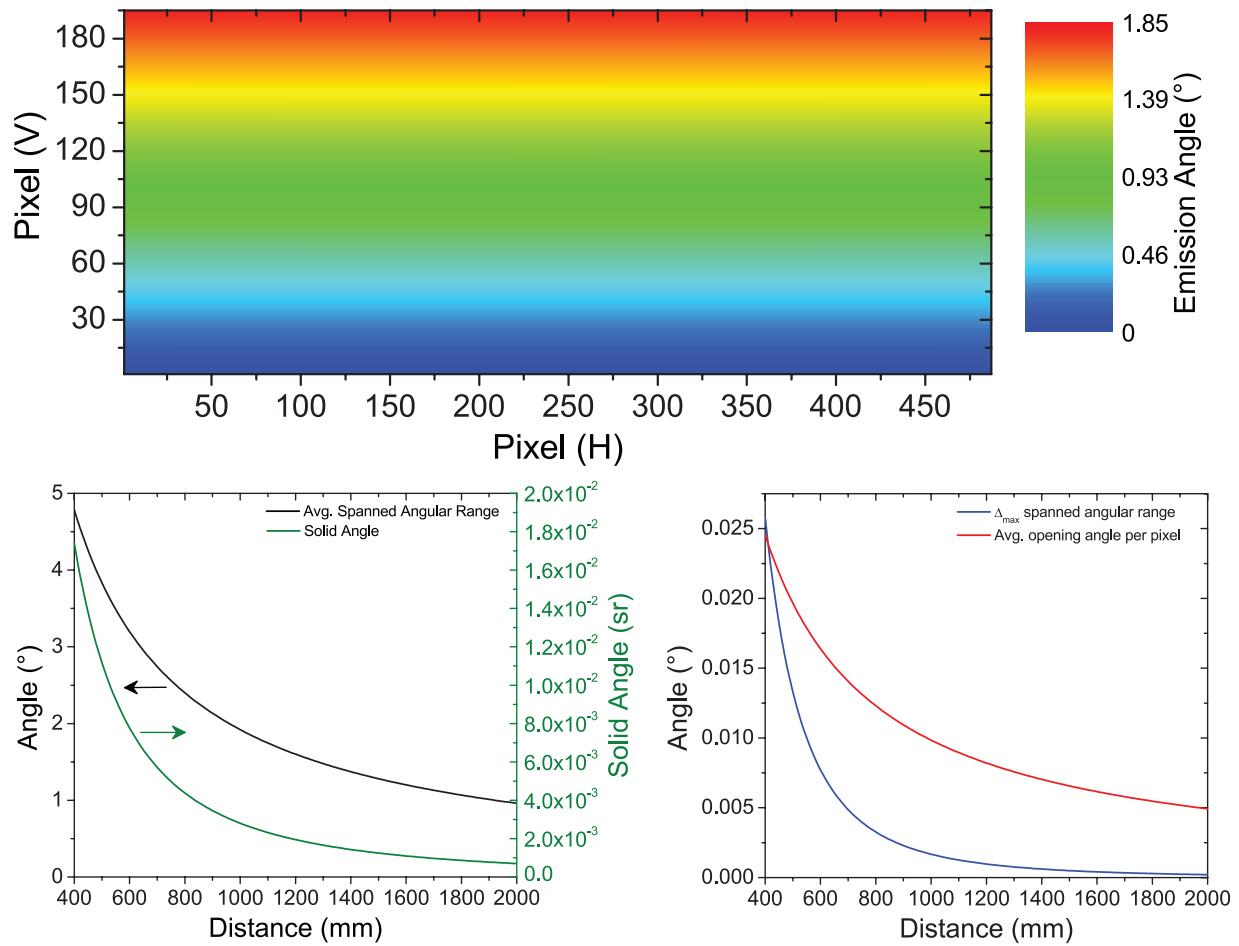


FIG. 3. Setup characterization for different parameters. The dispersion of the grazing emission angles over the active detector area is shown in the upper panel for the selected sample-to-detector distance of 106 cm at which the measurements were realized. Because of the large sample-to-detector distance, the variation of the emission angle along a detector row is small enough to allow for a binning of the recorded intensity values, thus an increased solid angle of detection per emission angle, without deteriorating the angular resolution. The maximum difference in the sustained emission angle varies linearly from 0° to 0.001° along the detector height. The spanned range in grazing emission angles and the overall solid angle of detection depend for a given detector height on the sample-to-detector distance (lower left panel). The angular resolution is mainly determined by the opening angle per pixel and the maximum difference in the spanned grazing emission angle range between the different detector columns, both factors depending pronouncedly on the sample-to-detector distance (lower right panel).

Based on above calculations and Fig. 3, a sample-to-detector distance of about 100 cm was found to be the best compromise for the present experimental setup. Finally, the detector was placed at a distance of 106 cm from the sample. Considering the selected sample-to-detector distance and the detector extension, the relative change in the distance of the different pixels to the source point is less than 0.15%. For the selected sample-to-detector distance and orientation of the PILATUS detector, the average covered angular range was 1.812° , the vertical opening angle per pixel was 0.00929° , and the solid angle per covered emission angle unit was 1.28×10^{-5} sr. The overall solid angle of detection with which the angular intensity profiles were acquired was 2.50×10^{-3} sr. Because of the large sample-to-detector distance compared to the detector dimensions, the maximum differences in the covered angular range for the different pixels and detector columns are on a relative scale at most of the order of 10^{-3} . Thus, it can be assumed that the dependencies of the opening angle per pixel on the pixel indexes j and k can be safely neglected.

The spanned range in emission angles per pixel as well as the sample-to-detector distance were verified by a sample rotation by means of the goniometer head around an axis which was parallel to the sample surface, which passed through the center of the spot irradiated by the incident beam and which was perpendicular to the normal of the detector surface. This allowed also to fix the 0° emission angle position along the angle dispersion axis. The intensity modulation of the experimental GEXRF profiles allowed to control the alignment of the detector with respect to the sample surface plane and thus to avoid any smear of the angular resolution due to a misalignment of the detector surface around its normal.

The angular resolution of the setup was experimentally found to be about 0.015° , thus comparable to the best reported angular resolutions for other GEXRF setups.⁶ The main contribution is given by the vertical opening angle per pixel. Other contributions are due to the discussed variation of the emission angle along a row of pixels (the maximum difference in the sustained emission angle in a pixel row being 0.001°),

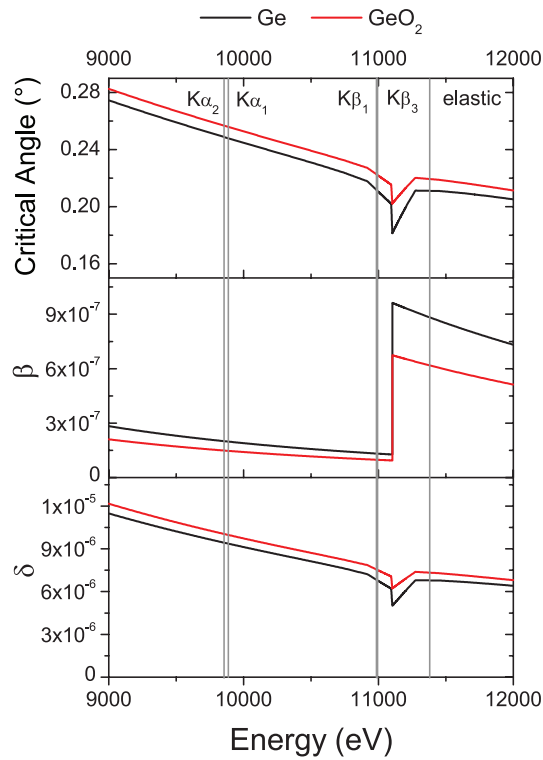


FIG. 4. Energy dependence for Ge of the real part (scattering properties) and the imaginary part (absorption properties) of the complex refractive index as well as the critical angle (from bottom to top). The vertical bars indicate the energy of the main emission lines and the energy of the incident beam. The linewidths of the $K\alpha$ lines being below 3 eV and the ones of the $K\beta$ about 4.2 eV, the change for each emission line in the optical properties can be estimated.

the extension of the sample surface area irradiated by the incident beam and also the linewidth of the different fluorescence lines has to be considered. The former contribution can be assessed by geometrical means and is much smaller than the calculated variation of the emission angle along a horizontal pixel row for a point source. Indeed, the dimensions of the irradiated sample surface are much smaller than the detector dimension. The latter contribution can be estimated from the variation of the critical angle over the linewidth of the studied XES signal. In a first approximation, valid in the energy regime below the absorption edge of the involved XES transition, the relative change in the critical angle over the linewidth ΔE can be estimated by $\frac{\Delta\theta_c}{\theta_c} \approx \frac{\Delta E}{E}$ (see Fig. 4). For the K emission lines the relative change in energy over the linewidth is about 5×10^{-4} . A further factor which could broaden the angular resolution is the probed sample depth which varies with the grazing emission angle.²⁸ However, the vertical size of the detector pixels is much larger, thus this factor can be safely neglected.

III. EXPERIMENTAL MEASUREMENTS

In the following, a few experimental examples of GEXRF profiles acquired with the presented setup will be presented together with an analysis of the data. Namely, the experimental data for a Ge bulk sample, a V- and a Cr-layered Si wafer as

well as two different Ga-implanted Ge wafers will be shown. In the presented setup, the GEXRF profiles of the different XES lines which were excited were acquired in a single measurement and could not be separated from each other, unlike in other reported setups. In the latter either a dispersive element or a silicon drift detector (SDD) is used in order to perform the measurement on a single x-ray emission line (within the possibilities given by the energy resolution of the detection setup). Indeed, the PILATUS detector does not allow for a direct energy discrimination of the recorded x-ray photons, only a threshold for the minimum energy of an x-ray photon can be set. Thus, all the x-ray energies above the detector threshold have to be considered. Consequently, the analysis of the measured GEXRF profile has to be adapted in order to consider all the XES lines of the different elements in the sample having an absorption edge below the energy of the incident synchrotron beam and an energy above the detector threshold. The threshold was set for the presented measurements to 4.25 keV. For the mentioned samples only the K emission lines had to be considered. The advantage of acquiring the GEXRF profiles from different x-ray emission lines simultaneously in a single measurement was a higher overall intensity yield allowing for faster measurements. Moreover, the acquired GEXRF profile contained more information since the contribution of different emission lines can be regarded as the combination of different GEXRF datasets.

When acquiring the GEXRF profiles, the detector was not set up in order to have the 0° emission angle on the bottom pixel row but several pixel rows above it. This allowed to measure the scattering background in parallel to the GEXRF profile and to correct the latter for the air scattering inherent to the measurement because of the large sample-to-detector distance. The background correction was realized by subtracting the average intensity per pixel recorded in the detector area below the 0° emission angle. Indeed, the scattering background was found to be constant in the direction along which the emission angle is dispersed.

The measured GEXRF profiles were analyzed on the basis of the formalism presented by Urbach and de Bokx.^{10,29} In the latter, the intensity dependence on the emission angle for a given XES line is obtained by considering the contribution of the emitting atoms. Physical phenomena influencing the detected XES intensity are directly taken into account and explicit analytic expressions for the angular intensity profile are obtained. This is advantageous for the interpretation of the experimental data. The formalism had, however, to be adapted to the shallow incidence angle and the simultaneous acquisition of multiple XES lines. Moreover, the elastic, i.e., coherent, scattering from the sample had also to be considered. The different individual GEXRF profiles $I_j(\varphi_e, \lambda_e^j)$ were multiplied by their normalized relative intensity RI_j and summed together

$$I(\varphi_e) = \sum_{j=1}^m RI_j \times I_j(\varphi_e, \lambda_e^j) \quad \text{with} \quad \sum_{j=1}^m RI_j = 1, \quad (5)$$

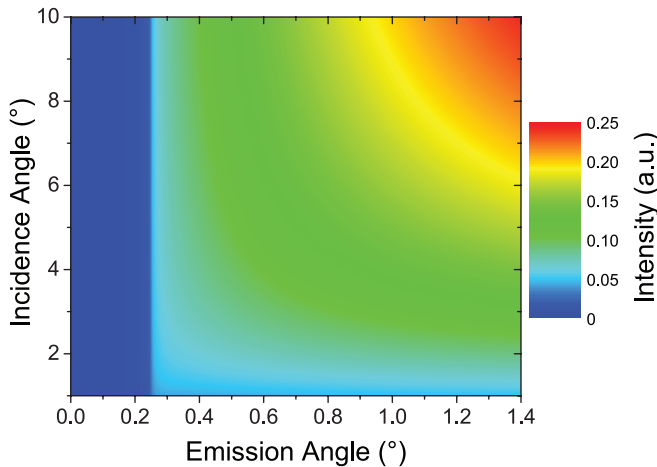
where m stands for the number of different photon energies which were recorded (XES lines and elastic scattering), λ_e

for the wavelength of the considered emission energy, and φ_e for the grazing emission angle.

A. Bulk sample

For the Ge bulk sample the $K\alpha_1$, $K\alpha_2$, $K\beta_1$, and $K\beta_3$ as well as the elastic peak had to be considered when analyzing the recorded GEXRF angular intensity profile, the relative intensity ratios of these 5 contributions being known.³⁰ The contribution of the elastic peak with respect to the overall contribution of the fluorescence lines was estimated from the different atomic cross-sections for the K-shell photoelectric absorption and the coherent scattering. The cross-sections can be considered as being proportional to the probability for the K-shell ionization and the subsequent emission of a fluorescence photon (taking the fluorescence factor into account), respectively, the elastic scattering of an incident photon. The relative change with the x-ray energy in the transmission through air on the path from the sample to the detector was taken into account as well while the detector efficiency could safely be considered to be uniform in the x-ray energy range of interest for the different measurements. Moreover, calculations reveal a quite pronounced dependence of the GEXRF profile on the shallow incidence angle (see Fig. 5, left panel). Indeed, the incidence angle has an influence on the probed depth volume for emission angles above the critical angle for the emitted x-rays. The exact value of the incidence angle ($\varphi_i = 2.769^\circ \pm 0.007^\circ$) was extracted from the fit of the measured Ge GEXRF profile. Thanks to the reference holder the incidence angle was identical for the other samples. The experimental GEXRF profile for a bulk sample is described by means of Eq. (5) where the individual contributions are given by

$$I_j(\varphi_e, \lambda_e^j) = |t_{\text{bulk} \nearrow \text{air}}(\lambda_e^j)|^2 \times \frac{1 - e^{-(2\text{Im}(k_{\text{bulk}}(\lambda_e^j)) + k_{\text{bulk}}(\lambda_i)\rho_{\text{bulk}})T_{\text{bulk}}}}{2\text{Im}(k_{\text{bulk}}(\lambda_e^j)) + k_{\text{bulk}}^i(\lambda_i)\rho_{\text{bulk}}}. \quad (6)$$



In Eq. (6) the first factor stands for the change in the field strength of the emitted radiation upon the transition of the interface separating the sample volume from the outside and the fraction with the exponentials accounts for the absorption of the incident and emitted x-ray photons inside the sample. In the subindex, the first named medium indicates from which side the emitted radiation is incident on the interface and the arrow indicates an upward or a downward propagation towards the refracting interface. The density is denoted by ρ_{bulk} , the thickness by T_{bulk} , and the wavelength of the incident radiation by λ_i . The different factors in Eq. (6) are defined as follows:

$$t_{\text{bulk} \nearrow \text{air}}(\lambda_e^j) = \frac{k_{\text{air}}(\lambda_e^j)}{k_{\text{bulk}}(\lambda_e^j)} \frac{\sqrt{n_{\text{bulk}}^2(\lambda_e^j) - \cos^2 \varphi_e}}{\sin \varphi_e + \sqrt{n_{\text{bulk}}^2(\lambda_e^j) - \cos^2 \varphi_e}},$$

$$k_{\text{air}}(\lambda_e^j) = \frac{2\pi}{\lambda_e^j} \sin \varphi_e,$$

$$k_{\text{bulk}}(\lambda_e^j) = \frac{2\pi}{\lambda_e^j} \sqrt{n_{\text{bulk}}^2(\lambda_e^j) - \cos^2 \varphi_e},$$

$$k_{\text{bulk}}^i(\lambda_i) = \frac{2\pi}{\lambda_i} \sqrt{n_{\text{bulk}}^2(\lambda_i) - \cos^2 \varphi_i}.$$

B. Layered samples

In the case of layered samples with thin (1-10 nm) or medium (10-100 nm) thicknesses, the extinction depth is for emission angles above the critical angle larger than the layer thickness. A shallow incidence angle will thus not reduce the probed depth region in the layer as it was the case for the bulk sample but ensure a more efficient excitation of the XES signal from layer atoms and an improved signal-to-background ratio. GEXRF measurements on layered samples are reported in Refs. 6, 8, 27, and 31–34.

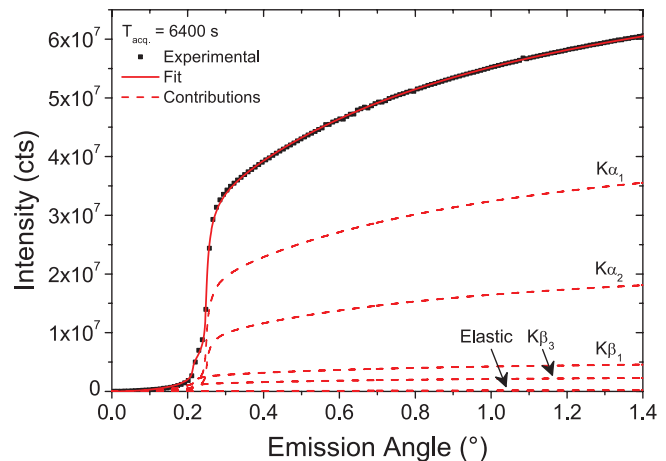


FIG. 5. In the left panel the dependence on the synchrotron beam incidence angle of the theoretical GEXRF profile for a bulk Ge sample as calculated with Eqs. (5) and (6) for the Ge K emission lines and the elastic contribution is shown. It can be seen that the aspect ratio depends significantly on the shallow incidence angle. The exact value of the probing beam incidence angle was deduced from a fit of the experimental GEXRF profile of the bulk Ge wafer (right panel), the individual contributions of the different emission lines and the elastic line are displayed as dashed lines.

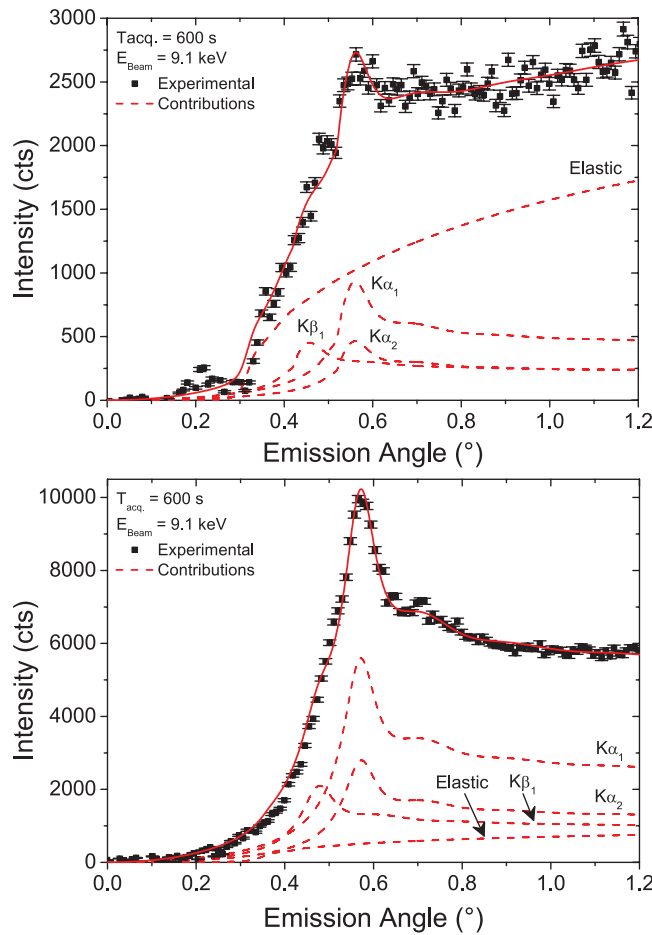


FIG. 6. Fit of the experimental GEXRF profiles for a V-layered Si sample (top panel) and a Cr-layered Si sample (bottom panel). A layer thickness of 23.2 ± 0.9 nm was fitted for the V layer and of 22.1 ± 0.2 for the Cr layer. The individual contributions of the V, respectively, Cr $K\alpha_1$, $K\alpha_2$, $K\beta_1$, and the elastic line are displayed as dashed lines. While for the characteristic lines obviously only the layer volume needed to be considered, the whole sample volume needed to be considered for the elastic line (see text). The characteristic lines of the bulk Si were not recorded because they were too low in energy.

The individual contributions from the layer part of the sample ($K\alpha_1$, $K\alpha_2$, $K\beta_1$, and the elastic line) when fitting the V layered Si wafer and the Cr layered Si wafer (Fig. 6) by means of Eq. (5) are defined as follows:

$$\begin{aligned}
 I(\varphi_e, \lambda_e^j) &= |t_{\text{lay.} \nearrow \text{air}}(\lambda_e^j)|^2 \\
 &\times \frac{1 - e^{-(2\text{Im}(k_{\text{lay.}}(\lambda_e^j)) + k_{\text{lay.}}(\lambda_i)\rho_{\text{lay.}})T_{\text{lay.}}}}{2\text{Im}(k_{\text{lay.}}(\lambda_e^j)) + k_{\text{lay.}}(\lambda_i)\rho_{\text{lay.}}} \\
 &\times \frac{1 + |r_{\text{lay.} \searrow \text{bulk}}(\lambda_e^j)|^2 e^{-2\text{Im}(k_{\text{lay.}}(\lambda_e^j))T_{\text{lay.}}} + \Psi(\varphi)(\lambda_e^j)}{|1 - r_{\text{lay.} \nearrow \text{air}}(\lambda_e^j)r_{\text{lay.} \searrow \text{bulk}}(\lambda_e^j)e^{-2ik_{\text{lay.}}(\lambda_e^j)T_{\text{lay.}}}|^2},
 \end{aligned} \quad (7)$$

where $\Psi(\varphi_e)$ corresponds to a correction term and the reflection factors on the two interfaces present in a layered sample

are given by

$$\begin{aligned}
 r_{\text{lay.} \nearrow \text{air}} &= \frac{\sqrt{n_{\text{lay.}}(\lambda_e^j)^2 - \cos^2 \varphi_e} - \sin \varphi_e}{\sqrt{n_{\text{lay.}}(\lambda_e^j)^2 - \cos^2 \varphi_e} + \sin \varphi_e}, \\
 r_{\text{lay.} \searrow \text{bulk}} &= \frac{\sqrt{n_{\text{lay.}}(\lambda_e^j)^2 - \cos^2 \varphi_e} - \sqrt{n_{\text{bulk}}(\lambda_e^j)^2 - \cos^2 \varphi_e}}{\sqrt{n_{\text{lay.}}(\lambda_e^j)^2 - \cos^2 \varphi_e} + \sqrt{n_{\text{bulk}}(\lambda_e^j)^2 - \cos^2 \varphi_e}},
 \end{aligned}$$

while the transmission factor $t_{\text{lay.} \nearrow \text{air}}(\lambda_e^j)$ and the amplitudes of the wavevectors are defined in analogy to the bulk example. With respect to a bulk sample (Eq. (6)), a third factor has to be considered in Eq. (7) for layered samples when calculating or fitting GEXRF profiles. This factor takes into account interferences of the emitted x-ray photons. The interferences are due to the fact that the photons emitted within the layer can be, with a certain probability given by the reflection coefficients, reflected on either of the interfaces formed by the layer with the neighboring optical media. Thus, there is more than one possible emission path towards the detector, especially for emission angles close or in-between the critical angles for the air-layer and the layer-bulk interfaces. Depending on the difference in the path length towards the detector, emitted photons of a given wavelength which follow different emission paths interfere constructively.¹⁰ Thus, an interference pattern may be observed in the GEXRF angular intensity profile.^{6,8,27,31–33} The interference pattern and the shape of the GEXRF profile in general depend significantly on the layer thickness and are thus a quite sensitive probe of the layer thickness. Eventually information on the layer density, chemical changes or the roughness can as well be extracted from the GEXRF profile.⁶ Together with the layer thickness the former two parameters allow for a quantification without using a reference sample or calibrated instrumentation.⁶

From the fit of the experimental data the layer thickness of V, respectively, Cr, could be extracted (Fig. 6). With respect to an eventual surface oxidation no clear evidence was found, while the density was within 1%-2% equal to the bulk value and a layer surface roughness of about 1 nm was retrieved. In the fit of the experimental data with Eqs. (5) and (7) an additional component had to be added, the elastic scattering from the bulk which has an unknown relative intensity with respect to the layer contributions accounted for in Eq. (7). Thus, the intensity contribution of the elastic scattering was used as an additional fitting parameter while the evolution with the grazing emission angle for the bulk contribution was modeled by

$$\begin{aligned}
 I(\varphi_e) &\approx |t_{\text{bulk} \nearrow \text{lay.}}(\lambda_e)t_{\text{lay.} \nearrow \text{air}}(\lambda_e)|^2 \\
 &\times e^{-(2\text{Im}(k_{\text{lay.}}(\lambda_e) + k_{\text{lay.}}(\lambda_i)\rho_{\text{lay.}}(\lambda_e))T_{\text{lay.}})} \\
 &\times \frac{1 - e^{-(2\text{Im}(k_{\text{bulk}}(\lambda_e) + k_{\text{bulk}}(\lambda_i)\rho_{\text{bulk}})T_{\text{bulk}})}}{2\text{Im}(k_{\text{bulk}}(\lambda_e) + k_{\text{bulk}}(\lambda_i)\rho_{\text{bulk}})} \\
 &\times \frac{1}{|1 - r_{\text{lay.}(\lambda_e) \nearrow \text{air}}(\lambda_e)r_{\text{lay.} \searrow \text{bulk}}(\lambda_e)e^{-2ik_{\text{lay.}}(\lambda_e)T_{\text{lay.}}}|^2},
 \end{aligned} \quad (8)$$

where

$$t_{\text{bulk} \nearrow \text{lay.}}(\lambda_e) = \frac{k_{\text{lay.}}(\lambda_e)}{k_{\text{bulk}}(\lambda_e)} \times \frac{\sqrt{n_{\text{bulk}}^2(\lambda_e) - \cos^2 \varphi_e}}{\sqrt{n_{\text{lay.}}^2(\lambda_e) - \cos^2 \varphi_e} + \sqrt{n_{\text{bulk}}^2(\lambda_e) - \cos^2 \varphi_e}}.$$

In Eq. (8) the incident wavelength is equal to the emitted one since the elastic scattering is considered but for the sake of comprehensibility different labels were used. The XES signal from the Si wafer underneath the layer did not need to be considered because of the detector threshold (and absorption in air). The elastic contribution from the bulk beneath the layer was quite important (Fig. 6). With respect to Eq. (6) the presence of the layer on the top of the bulk volume has to be considered in the transmission and absorption factors. In addition, possible reflections have to be considered with a third factor. Only contributions with an even number of reflections (once the x-rays emitted from within the bulk have penetrated into the layer) need to be accounted for.

C. Ion-implanted samples

For the Ga-implanted Ge layers the individual contributions of the characteristic Ga emission lines ($K\alpha_1$, $K\alpha_2$, $K\beta_1$, and $K\beta_3$) are defined by

$$I(\varphi_e, \lambda_e^j) = |t_{\text{bulk} \nearrow \text{air}}(\lambda_e^j)|^2 \times \int_0^{T_{\text{bulk}}} f(z) \times e^{-(2\text{Im}(k_{\text{imp}}(\lambda_e^j)) + k_{\text{bulk}}(\lambda_e^j) \rho_{\text{bulk}})z} dz, \quad (9)$$

where $f(z)$ stands for the dopant depth concentration distribution (the depth axis being labeled z and being perpendicular to the sample surface). Because of the low dopant concentration the refractive index in the norm of the different wavevectors was defined for a pure Ge bulk. Indeed, the Ga dopant concentration (10^{15} atoms/cm²) was considered to be sufficiently low to not alter the optical properties of the Ge bulk. Like for the pure bulk sample only one refracting interface and thus no interference fringes have to be considered. A measurement above the Ge K edge was performed in order to verify the calibration for the incidence angle and the emission angles realized with a pure Ge wafer (Fig. 5), thus the reproducibility from one sample to another. For the GEXRF measurements of the Ga dopant the characteristic lines of the Ge bulk

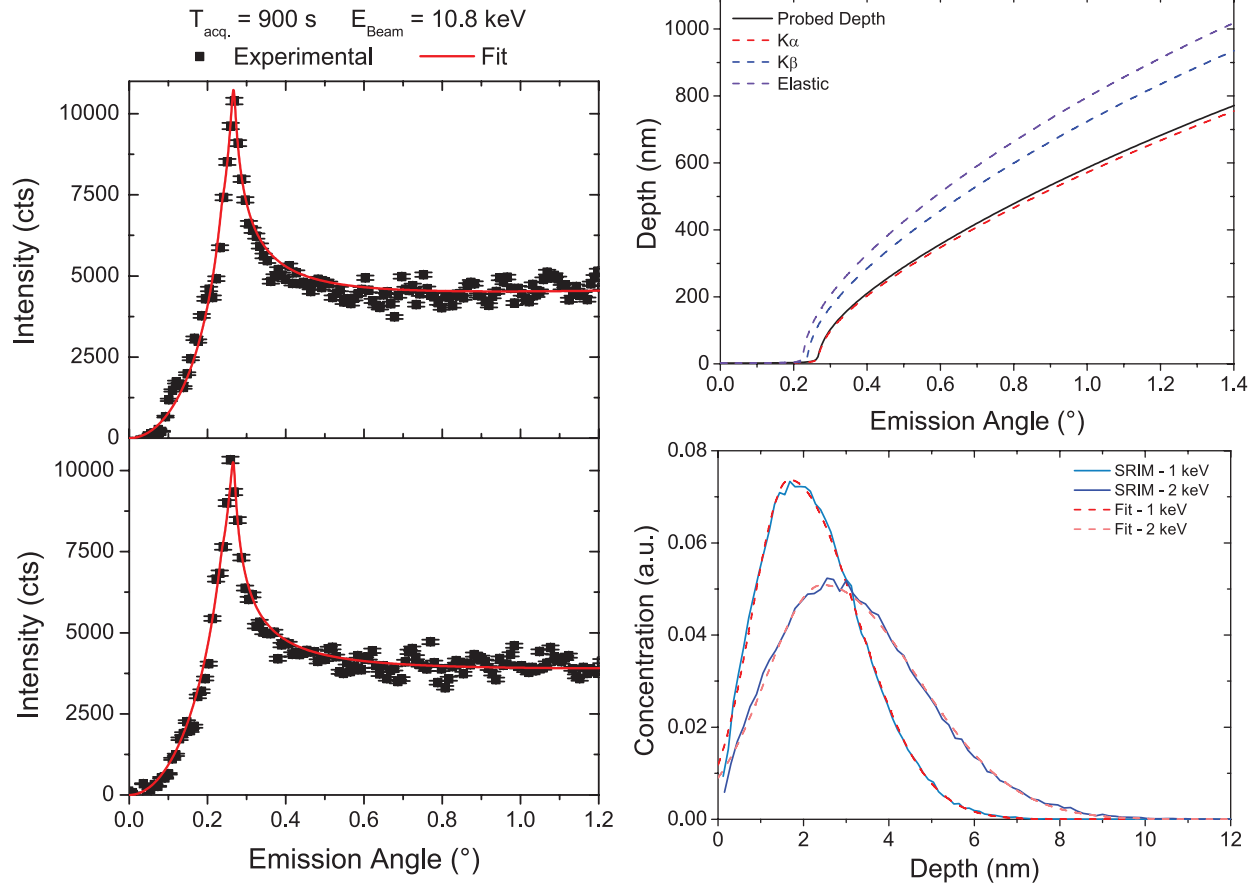


FIG. 7. The experimental GEXRF profiles for Ga-implanted Ge wafers (implantation energies of 1 and 2 keV, bottom to top) are displayed on the left, together with the fitted and the theoretical curves. The results from the fit are shown in the bottom right panel and compared to theory. In the right top panel, the dependence of the probed depth on the grazing emission angle is plotted for the different emission lines and for the weighted combination in order to illustrate the depth-sensitive character of GEXRF.

did not need to be accounted for since the experimental data were acquired at a synchrotron beam energy below the Ge K edge (11.103 keV). Moreover, the elastic contribution from the sample was corrected for by a measurement below the Ga K edge (10.367 keV). This allowed to record the shape of the background contribution from the elastic peak and, taking into account the different beam energies (once below, once above the Ga K edge) and hence the different critical angles for the elastic line, to subtract it from the measurement above the Ga K edge. In addition, the contribution of x-ray emission lines from an eventual contaminant in the sample matrix could be excluded. Consequently, only the contribution from the characteristic emission lines of Ga needed to be considered when fitting the experimental data.

From the experimental GEXRF profiles the depth dependent distribution $f(z)$ of the dopants can be retrieved. This has been demonstrated with other GEXRF setups.^{8,35} A comparison of depth-profiling for Al-implanted samples with GIXRF, respectively, GEXRF can be found in Ref. 36.

In order to retrieve the depth distribution of the Ga dopants from the experimental GEXRF profiles (Fig. 7) the depth distribution $f(z)$ of Ga in a Ge matrix was calculated for different implantation energies by means of the SRIM³⁷ program. This allowed, first, to find out which analytical curve describes best the dopant depth distribution, in the present case a half-joined Gaussian distribution, and, second, to extract the dependence on the implantation energy of the different parameters describing the analytical function. When fitting the experimental GEXRF profile with Eqs. (5) and (9), a single free parameter, the implantation energy, was sufficient to describe the dopant depth distribution. The result from the fit of the experimental data is displayed, together with the dependence of the probed depth on the grazing emission angle, in Fig. 7.

IV. CONCLUSION AND PERSPECTIVES

In summary, the arrangement for a scanning-free GEXRF setup by dispersing the grazing emission angles along one of the dimensions of a two-dimensional position-sensitive area detector was presented. The second detector dimension allowed to increase the solid angle of detection for each emission angle. This in combination with the fact that the XES intensity did not need to be recorded sequentially for the different emission angles, as in the common, scanning-based GEXRF setups, allows for short measurement times. The main properties of the scanning-free GEXRF setup, like the covered range of grazing emission angles, the angular resolution, the solid angle of detection, and the dependences on the sample-to-detector distance, the pixel size in the dispersion direction and the area of the 2D-detector, were presented and discussed. The most important interplay is the one between the angular resolution, which should be sufficient to resolve eventual interference fringes, and the sample-to-detector distance, respectively, the pixel size. A position-sensitive detector (1D or 2D) with a smaller pixel size would allow for a more compact setup configuration. The absorption in air on the path towards the detector and also the scattering background would be diminished if the experiment can be per-

formed in a He or vacuum environment. The presented setup can be realized with other two-dimensional, position-sensitive area detectors than the PILATUS as well. A CCD for example would offer the possibility for energy discrimination, thus a polychromatic excitation source for the XES signal could be used, respectively, the contribution of different elements to the measured signal could be treated separately. However, with CCD detectors, a possible blooming effect may deteriorate the angular resolution.

Measurements on a bulk, a layered, respectively, and ion-implanted samples served as illustrative examples for the possibilities offered by the presented scanning-free GEXRF configuration. A combination of the setup with other x-ray techniques (GIXRF, x-ray reflectometry, or x-ray absorption techniques) should be quite straightforward, alternatively an implementation into a setup using complementary surface-sensitive techniques is also realistic. In the case of combinations with other scanning-based techniques, a nonsequential acquisition of the GEXRF profiles is especially advantageous. The setup is in principle not bound to a synchrotron source but is also suitable for laboratory schemes. Configurations with laboratory sources for the excitation of the XES signal (x-ray tubes, electron guns) can certainly be realized. In comparison to GIXRF, a simpler arrangement can be envisaged since no additional elements in-between the source and the sample are needed in order to confine the monochromatic x-ray beam to individual, well-defined grazing incidence angles. Only a position-sensitive detector and a sufficient sample-to-detector distance are required. The latter depends mainly on the pixel size and influences the angular resolution. One of the main advantages of GEXRF is that the full flux offered by the excitation source can be profited from as long as the incident radiation is confined to the sample. In combination with sufficiently intense (pulsed) x-ray sources, single-shot GEXRF or dynamical studies by means of GEXRF could be thought about. Indeed, the use of the scanning-free GEXRF setup at an x-ray free electron laser (XFEL) is conceivable since the grazing emission geometry is insensitive to the energy jitter of the XFEL beam. Furthermore, in combination with micro-sized excitation sources and a normal incidence configuration (for reasons of positional resolution) lateral surface mapping applications of the surface-near sample region are also conceivable, the advantage of the presented setup being that the grazing emission angles do not need to be scanned separately. In principle, 3D measurements could be realized since GEXRF is a depth-sensitive technique. The presented scanning-free GEXRF setup shows the potential for the realization of new applications with GEXRF.

ACKNOWLEDGMENTS

We acknowledge the Swiss Light Source (SLS) at the Paul Scherrer Institut for provision of beam-time and U. Flechsig and A. Jaggi of the X05DA (Optics) beamline, where the presented setup and the appendant measurements were realized, for their kind help in the preparation of the experiment.

¹N. Alov, *Inorg. Mater.* **47**, 1487–1499 (2011).

²F. Meirer, A. Singh, P. Pianetta, G. Pepponi, F. Meirer, C. Strel, and T. Homma, *TrAC, Trends Anal. Chem.* **29**, 479 (2010).

- ³A. von Bohlen, *Spectrochim. Acta, Part B* **64**, 821 (2009).
- ⁴P. Wobrauschek, *X-Ray Spectrom.* **36**, 289 (2007).
- ⁵K. N. Stoev and K. Sakurai, *Spectrochim. Acta, Part B* **54**, 41 (1999).
- ⁶Y. Kayser, J. Szlachetko, D. Banaś, W. Cao, J.-Cl. Dousse, J. Hoszowska, A. Kubala-Kukuś, and M. Pajek, *Spectrochim. Acta, Part B* **88**, 136 (2013).
- ⁷M. Claes, P. de Bokx, and R. Van Grieken, *X-Ray Spectrom.* **28**, 224 (1999).
- ⁸P. de Bokx, C. Kok, A. Bailleur, G. Wiener, and H. Urbach, *Spectrochim. Acta, Part B* **52**, 829 (1997).
- ⁹R. S. Becker, J. A. Golovchenko, and J. R. Patel, *Phys. Rev. Lett.* **50**, 153 (1983).
- ¹⁰H. P. Urbach and P. K. de Bokx, *Phys. Rev. B* **53**, 3752 (1996).
- ¹¹T. Noma, A. Iida, and K. Sakurai, *Phys. Rev. B* **48**, 17524 (1993).
- ¹²A. Kubala-Kukuś, D. Banaś, W. Cao, J.-Cl. Dousse, J. Hoszowska, Y. Kayser, M. Pajek, M. Salomé, J. Susini, J. Szlachetko, and M. Szlachetko, *Phys. Rev. B* **80**, 113305 (2009).
- ¹³F. Meirer, G. Pepponi, C. Strel, P. Wobrauschek, and N. Zoeger, *J. Appl. Phys.* **105**, 074906 (2009).
- ¹⁴A. Kuczumow, M. Schmeling, and R. Van Grieken, *J. Anal. At. Spectrom.* **15**, 535 (2000).
- ¹⁵R. Pérez and H. Sánchez, *Rev. Sci. Instrum.* **68**, 2681 (1997).
- ¹⁶J. Yang, K. Tsuji, X. Lin, D. Han, and X. Ding, *Thin Solid Films* **517**, 3357 (2009).
- ¹⁷J. Szlachetko, D. Banaś, A. Kubala-Kukuś, M. Pajek, W. Cao, J.-Cl. Dousse, J. Hoszowska, Y. Kayser, M. Szlachetko, M. Kavčič, M. Salomé, and J. Susini, *J. Appl. Phys.* **105**, 086101 (2009).
- ¹⁸K. Tsuji, *Spectrochim. Acta, Part B* **60**, 1381 (2005).
- ¹⁹H. Schwenke, J. Knoth, P. A. Beaven, R. Kiehn, and J. Buhrz, in *10th Symposium on Total Reflection X-Ray Fluorescence Analysis and 39th Discussion Meeting on Chemical Analysis, Awaji Island, Hyogo, Japan, September 2003* [*Spectrochim. Acta, Part B* **59**, 1159 (2004)].
- ²⁰K. Tsuji, M. Huisman, Z. Spolnik, K. Wagatsuma, Y. Mori, R. Van Grieken, and R. D. Vis, *Spectrochim. Acta, Part B* **55**, 1009 (2000).
- ²¹B. Pollakowski, B. Beckhoff, F. Reinhardt, S. Braun, and P. Gawlitza, *Phys. Rev. B* **77**, 235408 (2008).
- ²²R. Klockenkämper, *Total Reflection X-Ray Fluorescence Analysis*, Chemical Analysis Vol. 140 (Wiley, 1997).
- ²³Y. C. Sasaki, Y. Suzuki, Y. Tomioka, and A. Fukuhara, *Phys. Rev. B* **48**, 7724 (1993).
- ²⁴Y. C. Sasaki, Y. Suzuki, Y. Tomioka, T. Ishibashi, I. Satoh, and K. Hirokawa, *Phys. Rev. B* **50**, 15516 (1994).
- ²⁵U. Flechsig, A. Jaggi, S. Spielmann, H. Padmore, and A. MacDowell, *Nucl. Instrum. Methods Phys. Res. A* **609**, 281 (2009).
- ²⁶C. Broennimann, E. F. Eikenberry, B. Henrich, R. Horisberger, G. Huelsen, E. Pohl, B. Schmitt, C. Schulze-Bries, M. Suzuki, T. Tomizaki, H. Toyokawa, and A. Wagner, *J. Synchrotron Radiat.* **13**, 120 (2006).
- ²⁷K. Tsuji, H. Takenaka, K. Wagatsuma, P. K. de Bokx, and R. Van Grieken, *Spectrochim. Acta, Part B* **54**, 1881 (1999).
- ²⁸P. Skyt, B. Galnander, T. Nyberg, J. Nordgren, and P. Isberg, *Nucl. Instrum. Methods Phys. Res. A* **384**, 558 (1997).
- ²⁹H. P. Urbach and P. K. de Bokx, *Phys. Rev. B* **63**, 085408 (2001).
- ³⁰L. Storm and H. I. Israel, *At. Data Nucl. Data Tables* **7**, 565 (1970).
- ³¹I. Koshelev, A. Paulikas, M. Beno, G. Jennings, J. Linton, M. Grimsditch, S. Uran, and B. Veal, *Oxid. Met.* **68**, 37 (2007).
- ³²M. L. Monaghan, T. Nigam, M. Houssa, S. D. Gendt, H. P. Urbach, and P. K. de Bokx, *Thin Solid Films* **359**, 197 (2000).
- ³³G. Wiener, S. J. Kidd, C. A. H. Mutsaers, R. A. M. Wolters, and P. K. de Bokx, *Appl. Surf. Sci.* **125**, 129 (1998).
- ³⁴K. Tsuji, S. Sato, and K. Hirokawa, *Rev. Sci. Instrum.* **66**, 4847 (1995).
- ³⁵Y. Kayser, D. Banaś, W. Cao, J.-Cl. Dousse, J. Hoszowska, P. Jagodziński, M. Kavčič, A. Kubala-Kukuś, S. Nowak, M. Pajek, and J. Szlachetko, *X-Ray Spectrom.* **41**, 98 (2012).
- ³⁶P. Hönicke, Y. Kayser, B. Beckhoff, M. Muller, J.-Cl. Dousse, J. Hoszowska, and S. H. Nowak, *J. Anal. At. Spectrom.* **27**, 1432 (2012).
- ³⁷J. F. Ziegler, in *Proceedings of the Sixteenth International Conference on Ion Beam Analysis, Albuquerque, NM, USA, 29 June–4 July 2003* [*Nucl. Instrum. Methods Phys. Res. B* **219–220**, 1027 (2004)].